

Radiative Efficiency of Disk Accretion in Individual SDSS QSOs

Shumei Wu^{1,2}, Youjun Lu^{1*}, Fupeng Zhang^{1,2}, & Ye Lu¹

¹*National Astronomical Observatories, Chinese Academy of Sciences, Beijing, 100012, China*

²*Graduate School of the Chinese Academy of Sciences, Beijing 100049, China*

11 April 2019

ABSTRACT

We estimate the radiative efficiency ϵ of individual type 1 SDSS QSOs by using their bolometric luminosities (L_{bol}) and accretion rates ($\dot{M}_{\bullet, \text{acc}}$), which may be related to the assembly histories and spins of the central massive black holes (MBHs). We estimate L_{bol} by using the empirical spectral energy distributions of QSOs and $\dot{M}_{\bullet, \text{acc}}$ by fitting the observed optical luminosity(/-ies) with the thin accretion disk model, assuming the MBH masses given by the virial mass estimator(s) ($M_{\bullet, \text{vir}}$). We find an apparent correlation between ϵ and $M_{\bullet, \text{vir}}$, which is strong at redshift $z \lesssim 1.8$, weak at $z \gtrsim 2$, and consistent with that found by Davis & Laor (2011) for 80 PG QSOs at $z \leq 0.5$. To investigate whether this correlation is intrinsic or not, we construct a mock sample of QSOs according to the true MBH mass and Eddington ratio distributions given in Kelly & Shen (2013). By comparing the results obtained from the mock sample with that from the SDSS sample, we demonstrate that the apparent $\epsilon - M_{\bullet, \text{vir}}$ correlation can be produced by and mainly due to the selection effects of the SDSS sample and the bias induced by the usage of $M_{\bullet, \text{vir}}$ as the true MBH mass. The mean value of ϵ of those SDSS QSOs are consistent with being a constant $\simeq 0.11 - 0.16$ at $0.3 \lesssim z \lesssim 4$. We conclude that the current SDSS QSO data is consistent with no strong intrinsic correlation between radiative efficiency and true MBH mass and no significant redshift evolution of radiative efficiencies.

Key words: accretion, accretion discs – black hole physics – galaxies: nuclei – galaxies: active – quasars: general

1 INTRODUCTION

Disk accretion of gaseous material onto a massive black hole (MBH) is believed to be the central engine of QSO and Active Galactic Nucleus (AGN¹; e.g., Krolik 1999). In the thin disk accretion scenario, the emergent spectrum of a QSO is mainly determined by several parameters, including the MBH mass (M_{\bullet}) and spin (a), the accretion rate (\dot{M}_{acc}), and the inclination angle (i) of the disk to the line of sight (e.g., Krolik 1999, see also Shakura & Sunyaev 1973; Novikov & Thorne 1973). Measuring the MBH mass (M_{\bullet}) and spin (a) for each individual QSOs is of fundamental importance and has been one of the major goals for the QSO and MBH studies. As illustrated by a number of studies (e.g., Gammie et al. 2004; Volonteri et al. 2005; King & Pringle 2006; King et al. 2008; Berti & Volonteri

2008; Volonteri et al. 2012), obtaining the statistical distributions of M_{\bullet} and a among QSOs is probably crucial for our understanding of the growth history of MBHs and the cosmic evolution of QSOs. In principle, M_{\bullet} , \dot{M}_{acc} and a can be estimated through the fitting of the multi-wavelength spectrum of each QSO by dedicated disk model(s) (e.g., Sun & Malkan 1989). However, it is practically not easy to estimate these parameters simultaneously with considerable accuracy, partly because of the complications in disk accretion model(s) and partly because of lack of measurements at the EUV to soft X-ray bands, where the disk emission is expected to be most prominent, for most QSOs. Alternative methods to estimate M_{\bullet} and a are necessary for understanding the evolution and assembly history of MBHs.

The mass of a MBH in a QSO can be estimated through the reverberation mapping (RM) technique (Blandford & McKee 1982), which is time consuming and currently is not possible for all QSOs. Fortunately, recent developments in measuring the masses of MBHs through the RM technique have resulted in some empirical scal-

* To whom correspondence should be addressed. Email: luyj@nao.cas.cn

¹ Hereafter, we do not distinguish AGN from QSO.

ing relations, i.e., the virial mass estimators, which offer simple ways to estimate the MBH mass of a QSO (e.g., Kaspi et al. 2000; Peterson et al. 2004; Vestergaard 2002; Vestergaard & Peterson 2006; Shen et al. 2008, 2011). Adopting these virial mass estimators, Shen et al. (2008, 2011) have obtained the MBH masses for most SDSS QSOs by using the QSO optical luminosities and the width of some broad emission lines (such as H β , CIV, and Mg II) in the QSO spectra.

If the MBH mass is known for a QSO, the absolute accretion rate \dot{M}_{acc} can be estimated based on the optical band luminosity by using the thin disk accretion model. The radiative efficiency is then obtained by $\epsilon = L_{\text{bol}}/\dot{M}_{\text{acc}}c^2$, where L_{bol} is the bolometric luminosity. The MBH spin a can be inferred from ϵ as ϵ is simply determined by a in the thin disk accretion model. With this method, it may be possible to indirectly infer the MBH spin and its distribution for a large sample of QSOs. (Note here that direct measuring the spins of MBHs through features like the broad Fe K α line is currently possible only for a limited number of cases (e.g., MCG-6-30-15 and a dozen of other AGNs; see Fabian et al. 2000; Risaliti et al. 2013; Reynolds 2013a,b; and reference therein).

Davis & Laor (2011) estimated ϵ for 80 PG QSOs (hereafter DL sample or DL QSOs) by adopting the above method and found that ϵ is strongly correlated with M_{\bullet} , i.e., $\epsilon \propto M_{\bullet}^{0.5}$, and they argued that such a correlation is unlikely induced by selection effects (Laor & Davis 2011, see also Chelouche 2013). If the above correlation is intrinsic, it might suggest that the spin of a big MBH is relatively larger than that of a small MBH and the growth histories of big MBHs are systematically different from that of small MBHs. However, Raimundo et al. (2012) argued that such a correlation is most likely an artifact of the small parameter space in both luminosity and redshift covered by the DL sample, and additional factors, such as the host galaxy and dust contamination, uncertainties in the bolometric luminosity estimations, may also bias the estimations of ϵ . Raimundo et al. (2012) concluded that the radiative efficiency itself cannot be accurately measured due to the large errors in the relevant observed parameters. Therefore, it is still not clear whether ϵ really intrinsically correlates with M_{\bullet} or not.

In this study, we extend the work of Davis & Laor (2011) to the type 1 SDSS QSOs, in order to further study the radiative efficiency of individual QSOs and its relation, if any, with MBH mass. Such a study should be helpful to identify various biases involved in the estimations of ϵ and address the question of whether ϵ correlates with M_{\bullet} or not, as the SDSS sample has many more QSOs and covers larger luminosity and redshift ranges compared to the DL sample.

This paper is organized as follows. In section 2, we introduce the SDSS QSO sample adopted in this study. In section 3, we first introduce the method to estimate the radiative efficiency and then obtain the radiative efficiency for individual type 1 SDSS QSOs. Similar to Davis & Laor (2011), we also find that the estimated radiative efficiency appears to be strongly correlated with the MBH virial mass at redshift $z \leq 0.5$. Such a strong correlation appears to exist for the SDSS QSOs at $z < 1.9$ but not at $z \gtrsim 2$. In section 4, we investigate various biases that could be involved in the ϵ estimations and the selection effects of the QSO sample, and adopt Monte Carlo simulations to generate mock

QSO samples to simulate the effects of these biases. We find that the current data is consistent with no mass and redshift dependence of ϵ . Conclusions are given in section 5.

2 SDSS QSO SAMPLE

A large number of QSOs have been detected by the SDSS. In the catalog of SDSS QSOs (DR7), 104,746 QSOs have i -band magnitude $M_i < -22$, at least one broad emission line broader than 1000km s^{-1} , and the estimations of the central MBH masses. About half of these QSOs (totally 57,959 QSO at $0.3 \leq z \leq 5$) were selected out to form a homogeneous, statistical sample, which is primarily a flux limited sample with i -band magnitude $m_i \leq 19.1$ at $z \leq 2.9$, $m_i \leq 20.2$ at $z > 2.9$ and an additional bright limit of $m_i \geq 15$ (Richards et al. 2002; Kelly & Shen 2013). Estimations of the MBH masses of the QSOs in this sample have been obtained by using the virial mass estimators based on scaling relationships calibrated for four different emission lines, i.e., H α , H β , Mg II, and CIV. These estimations, together with the optical band luminosities, for this QSO sample are given in Shen et al. (2011). We select the QSOs with $0.3 \leq z \leq 4$ in this sample to form our QSO sample (totally 56,691 QSOs) to be studied in this work, and these QSOs are denoted as the SDSS QSOs hereafter if not otherwise stated. With this homogeneous, statistical QSO sample, it is possible to study and model the selection effects and various biases involved in the estimations of the radiative efficiency of individual QSOs as the true MBH mass function and Eddington ratio distribution have also been estimated by Kelly & Shen (2013, see details in section 4).

The monochromatic luminosities are provided only at one or two wavelengths for most of the QSOs in the sample of Shen et al. (2011). For example, the monochromatic luminosities at 5100Å, 3000Å, and 1350Å are provided for QSOs with redshift $z < 0.9$, $0.35 < z < 2.25$, and $z > 1.5$, respectively. For those QSOs with $0.35 < z < 0.9$, there are two monochromatic luminosity measurements available at 5100Å and 3000Å, respectively; and for those QSOs with $1.5 < z < 2.25$, there are also two monochromatic luminosity measurements available at 3000Å and 1350Å, respectively. For other QSOs, only one monochromatic luminosity measurement is available, either at 5100Å for those with $z < 0.35$ or at 1350Å for those with $z > 2.25$.

3 RADIATIVE EFFICIENCIES OF DISK ACCRETION IN INDIVIDUAL SDSS QSOs

The radiative efficiency (ϵ) of the accretion process in a QSO may be estimated by using its bolometric luminosity (L_{bol}) and the accretion rate (\dot{M}_{acc}), i.e., $\epsilon = L_{\text{bol}}/\dot{M}_{\text{acc}}c^2$, if these two quantities can be (independently) accurately determined. Given the mass of the central MBH of a QSO and the QSO multi-wavelength spectrum, in principle, the accretion rate can be estimated by adopting dedicated disk accretion model(s); and the bolometric luminosity can also be estimated by integrating the QSO multi-wavelength spectrum. In this section, we will first estimate the mass accretion rate and the bolometric luminosity for individual SDSS QSOs, and then estimate the radiative efficiency ϵ .

3.1 Mass accretion rates \dot{M}_{acc}

In the standard disk accretion scenario, the multi-wavelength spectrum of a QSO is mainly determined by the mass and spin of the central MBH and the accretion rate (e.g., Krolik 1999, see also Shakura & Sunyaev 1973; Novikov & Thorne 1973). The masses of the central MBHs in most SDSS QSOs have been estimated through the virial estimators (e.g., Shen et al. 2008, 2011), while the MBH spins are still difficult to measure. The optical band luminosity of a QSO is dominated by the emission from the outer disk, and it is mainly determined by the accretion rate of the disk and less affected by the MBH spin (e.g., Krolik 1999; Davis & Laor 2011). Therefore, the accretion rate \dot{M}_{acc} of a SDSS QSO, with known MBH mass, can be estimated with reasonable accuracy by only matching the observed optical band luminosity(/-ies) L_{opt} with that predicted by an accretion disk model. Similar to Davis & Laor (2011), we adopt two different accretion disk models, i.e., the standard thin disk model and the TLUSTY model to estimate the mass accretion rate of individual SDSS QSOs as follows.

- The standard thin accretion disk model (hereafter the BB model). Here we adopt the relativistic standard thin disk model presented in Gierliński et al. (2001, see also Novikov & Thorne 1973, Page & Thorne 1974). In this model, the inner edge of the accretion disk is assumed to be the innermost stable circular orbit (ISCO), which is solely determined by the MBH spin, and no emission comes from the region within ISCO. The emergent spectrum is directly determined by the multi-temperature black body radiation integrated over the disk surface.

- The TLUSTY model (Hubeny et al. 2000; Hubeny & Lanz 1995). In this model, not only the relativistic effects are included, but also the disk vertical structure and the radiative transfer in the disk are simultaneously considered (for details, see Hubeny et al. 2000). In the TLUSTY model, the emergent spectrum from each annulus is first calculated and the full spectrum is obtained by integrating over the disk radius. Occasionally, the TLUSTY model could not converge for some specific parameter space, e.g., at large radius or extremely large/small accretion rate, possibly because the disk material in this situation is already quite cool and/or convection becomes important. In these cases, we simply replace the radiation of these annuli by black body radiation (see also discussions in Davis & Laor 2011).

These models have four parameters, i.e., the MBH mass M_{\bullet} and spin a , the accretion rate \dot{M}_{acc} , and the inclination angle i of the disk to the line of sight. The model spectrum estimated from the TLUSTY model may also depend on the choice of the α_{SS} -viscosity (Shakura & Sunyaev 1973), which is simply set to be $\alpha_{\text{SS}} = 0.01$ for all models as this parameter have little effect on the L_{opt} (e.g., see Davis & Laor 2011).

It is necessary to have some information about the other model parameters, i.e., M_{\bullet} , a and i , in order to estimate \dot{M}_{acc} with reasonable accuracy for a QSO by only using its monochromatic luminosities in a limited range of wavelengths. The MBH mass, M_{\bullet} , has been estimated for the majority of the SDSS QSOs by using the virial mass estimators but with uncertainties of 0.3 – 0.4 dex (e.g., Shen et al.

2008, 2011). The inner radius of an accretion disk is defined by the MBH spin a . The model spectra in the optical bands are not significantly affected by the setting of the disk inner edge although the disk radiation at higher frequency is indeed affected by it. If not otherwise stated, we simply adopt $a = 0.67$ in our following calculations, which corresponds to $\epsilon \sim 0.1$ in the standard disk model.² We adopt this spin value as reference since the global constraints on the mean radiative efficiency of QSOs suggest $\epsilon \sim 0.1 - 0.2$ (e.g., Yu & Tremaine 2002; Yu & Lu 2004; Marconi et al. 2004; Yu & Lu 2008; Shankar et al. 2009; Zhang et al. 2012; Shankar et al. 2013). For the inclination angle i , all QSOs in the sample of Shen et al. (2011) are type 1 QSOs, which presumably have small inclination angles with $\cos i$ in the range of 0.5 to 1. The exact value of i for each QSO cannot be constrained directly from the SDSS observations. In this section, we set a fixed value of $\cos i = 0.8$ for the fitting, with which the results obtained here can be directly compared with that found in Davis & Laor (2011) and Raimundo et al. (2012).

With the virial mass of a central MBH and the above settings on the MBH spin and inclination angle, it is possible to estimate the accretion rate for the QSO by matching the observed monochromatic luminosity in an optical band to the model ones. In the sample of Shen et al. (2011), the monochromatic luminosities are provided at two wavelengths for those QSOs with $0.35 < z < 0.9$ or $1.5 < z < 2.25$ (i.e., at 5100Å and 3000Å, or at 3000Å and 1350Å; see section 2). For these cases, the two estimates of the accretion rate generally differ by no more than 0.1 – 0.2 dex according to our calculations. We adopt the mean value of the two estimations of the accretion rate, obtained from the two monochromatic luminosity measurements, as the QSO accretion rate, and the uncertainty of this rate is $\lesssim 0.1$ dex, which may lead to an uncertainty of $\lesssim 0.1$ dex in the efficiency estimation. However, such an amount of uncertainty seem negligible compared with the biases induced by the usage of the virial mass as the true MBH mass as mainly discussed in section 4.1 below.

The obtained value of \dot{M}_{acc} for a QSO may be biased because of the usage of the virial mass as the true MBH mass and the fixed values for the MBH spin and the disk inclination angle here. The biases induced by these settings on \dot{M}_{acc} and consequently the ϵ estimations will be further analyzed in section 4.

3.2 Bolometric luminosities L_{bol}

It is necessary to estimate its bolometric luminosity with considerable accuracy to obtain the radiative efficiency ϵ of a QSO. For a QSO with multi-wavelength observations, its bolometric luminosity can be directly obtained by integrating its spectrum over the range from radio to hard X-ray but excluding the reprocessed radiation in the infrared. However, most SDSS QSOs have been observed only in a limited wavelength range, e.g., in the optical band. It may not be an appropriate way to directly convert the optical band luminosity to the bolometric luminosity according to a theoretical accretion disk model, as the radiation processes for high energy

² Alternatively adopting $a = 0.83$ (or $a = 0.96$), i.e., $\epsilon \sim 0.13$ (or 0.2), does not significantly affect the final results.

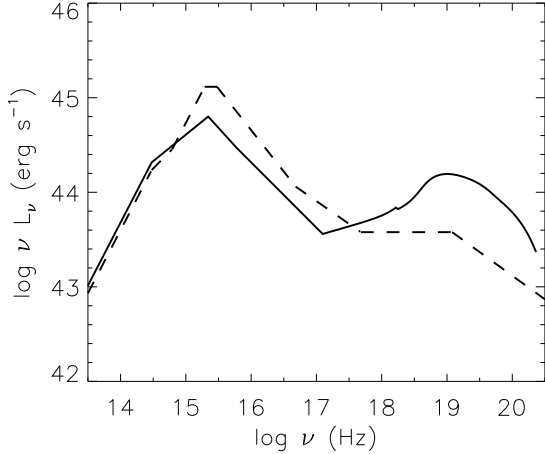


Figure 1. Schematic spectral energy density distribution (SED) adopted for a QSO with $L_{2500\text{\AA}} = 10^{44.5} \text{ erg s}^{-1}$. The solid and dashed lines show an example SED of that adopted in this study (see section 3.2) and that adopted in Davis & Laor (2011, see case A in section 3.1 therein), respectively.

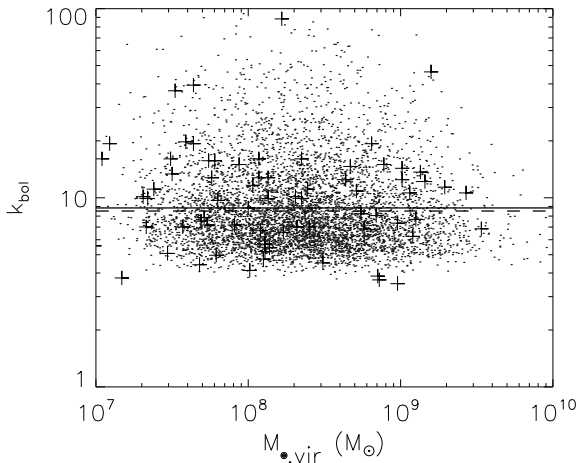


Figure 2. Bolometric corrections k_{bol} at 5100Å for the type 1 SDSS QSOs at redshift $z \leq 0.5$ (black dots; totally 5,786 SDSS QSOs) and the DL QSOs (black crosses; adopted from Davis & Laor 2011), respectively. Solid and dashed lines represent the mean value of $\log k_{\text{bol}}$ for the SDSS QSOs ($\langle \log k_{\text{bol}} \rangle = 0.95$) and the DL QSOs ($\langle \log k_{\text{bol}} \rangle = 0.93$), respectively.

photons (which contribute significantly to the total luminosity) emitted from the inner disk region are complicated and not fully understood (e.g., Krolik 1999). Here we adopt an empirical method to calculate the bolometric luminosity of individual QSOs by constructing a spectral energy distribution (SED) for individual QSOs based on some empirical relations obtained for small samples of QSOs, which is similar to that adopted in Hopkins et al. (2007) and Marconi et al. (2004, and see references therein).

The spectra or SEDs of individual QSOs are constructed as follows.

(i) In the optical-UV bands ($1\mu\text{m} < \lambda < 1300\text{\AA}$), the QSO spectrum is assumed to be a power law, and we assign the power-law index to each QSO according to a Gaussian distribution with mean $\alpha_{\text{opt}} = -0.44$ with scatter $\sigma_{\alpha_{\text{opt}}} = 0.125$ (see Vanden Berk et al. 2001). The spectrum is normalized to the monochromatic luminosity at 5100Å, i.e., $L_{5100\text{\AA}}$. (If $L_{5100\text{\AA}}$ is not available for some QSOs, we estimate it by extrapolation from $L_{3000\text{\AA}}$ or $L_{1350\text{\AA}}$).

(ii) In the UV wavelengths (1200Å–500Å), the QSO spectrum is also described by a power law, and we randomly assign the power-law index according to a Gaussian distribution with mean $\alpha_{\text{UV}} = -1.76$ with a scatter of $\sigma_{\alpha_{\text{UV}}} = 0.12$ (Telfer et al. 2002).

(iii) At the X-ray beyond 0.5keV, the spectrum is assumed to be a power law with an exponential cutoff at 500keV. We assign the photon index according to a Gaussian distribution with mean $\Gamma = -1.83$ and a scatter of $\sigma_{\Gamma} = 0.18$ for each QSO (Jin et al. 2012, see also Tozzi et al. 2006).

(iv) A reflection component is generated for each QSO by using the PEXRAV model (Magdziarz & Zdziarski 1995) in the XSPEC package with a reflection solid angle of 2π , inclination of $\cos i = 0.8$ and solar abundance.

(v) The X-ray spectrum is re-normalized to a given $\alpha_{\text{ox}} = -0.384 \log [L_{2500\text{\AA}}/L_{\nu}(2\text{keV})]$, and the points at 500Å and 50Å are connected with a power-law. The value of α_{ox} depends on luminosity, and we adopt the most recent determination by Lusso et al. (2010, see also Steffen et al. 2006), i.e., $\alpha_{\text{ox}} = -0.154 \log (L_{2500\text{\AA}}/\text{ergs}^{-1}\text{Hz}^{-1}) + 3.176$, with an intrinsic scatter of $\sigma_{\alpha_{\text{ox}}} = 0.18$.

(vi) At wavelengths longer than $1\mu\text{m}$, the QSO spectrum may be dominated by the emission from the dusty torus by re-processing the optical-UV-X-ray photons radiated from the inner disk, which should not be counted in the calculations of the bolometric luminosities of QSOs. We assume a power law continuum emission with slope 1/3, similar to that adopted in Davis & Laor (2011).

Figure 1 shows an example SED constructed for a QSO with $L_{2500\text{\AA}} = 10^{44.5} \text{ erg s}^{-1}$ according to the above prescription. As seen from Figure 1, the general SED adopted in this study (the solid line) is somewhat different from that adopted in Davis & Laor (2011, the dashed line), and the differences include (1) the reflection component of the X-ray emission due to the disk is considered in this study but not in Davis & Laor (2011); (2) our choice of the intrinsic X-ray continuum above 0.2 keV is also slightly different from that in Davis & Laor (2011); (3) the continuum slope at optical to UV band is set to be -0.44 in our study; but in Davis & Laor (2011) it is set to be -0.3 between $1\mu\text{m}$ and 4861\AA , -1 between 1549\AA and 1000\AA , and set to be the one measured for each QSO in the wavelength range from 4861\AA to 1549\AA and from 1000\AA to 0.2 keV, respectively. However, these differences do not lead to much difference in the bolometric corrections as shown in Figures 2 and 3.

By integrating over the constructed spectrum of each QSO in the sample according to the above prescription, we obtain its “bolometric luminosity”, and the distribution of the “bolometric luminosity” of these QSOs should statistically reflect the underlying real distribution of the sample. Given the bolometric luminosity, we also obtain the bolometric correction (BC) at 5100Å for each QSO with the luminosity measurement at 5100Å, i.e., $k_{\text{bol}} = L_{\text{bol}}/L_{5100\text{\AA}}$.

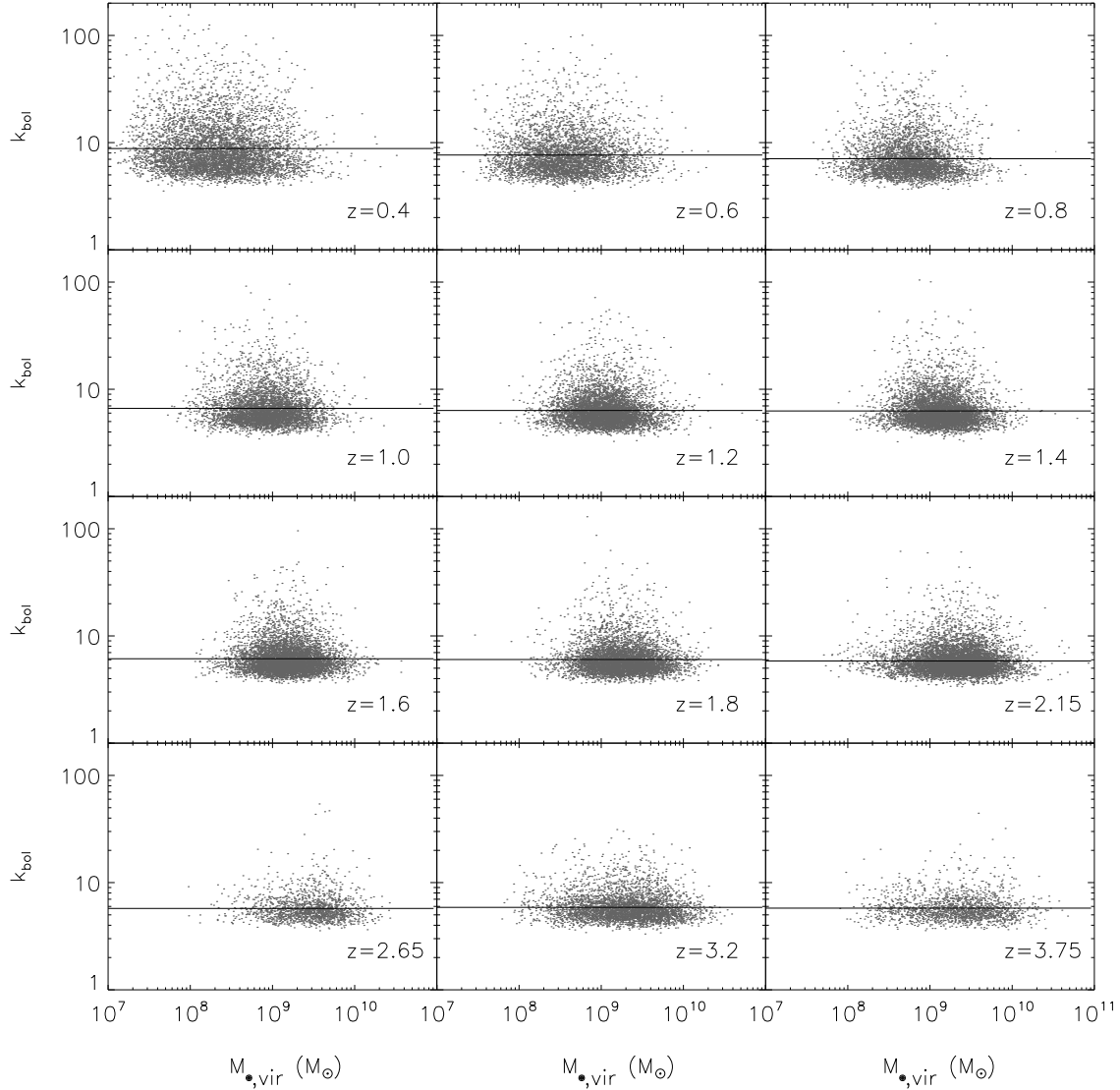


Figure 3. Bolometric corrections k_{bol} at 5100\AA for the type 1 SDSS QSOs in different redshift bins. The solid line represents the mean value of $\langle \log k_{\text{bol}} \rangle$ for the SDSS QSOs in each redshift bin. For those QSOs with monochromatic luminosities available at 3000\AA and/or 1350\AA , we obtain $L_{5100\text{\AA}}$ according to the empirical spectral energy distributions.

Figure 2 shows the BCs at 5100\AA obtained for the SDSS QSOs at redshift $z \leq 0.5$. As seen from Figure 2, the obtained BCs do not depend on $M_{\bullet, \text{vir}}$, which is consistent with the results obtained by Davis & Laor (2011) for a sub-sample of PG QSOs in a similar redshift range (the plus symbols in Figure 2). The range of the BCs for the SDSS QSOs is also roughly consistent with that for the DL sample. The mean logarithmic BC value of the DL QSOs is $\langle \log k_{\text{bol}} \rangle = 0.93$ with a scatter of $\sigma_{\log k_{\text{bol}}} \simeq 0.27$, while that of the SDSS QSOs is $\langle \log k_{\text{bol}} \rangle = 0.95$ with a scatter of $\sigma_{\log k_{\text{bol}}} \simeq 0.22$ (as shown by the solid and dashed lines in Figure 2, respectively). The mean value of the logarithmic BCs for the SDSS QSOs is slightly larger than that of the DL sample, which might be due to the choice of the empirical SED. For example, if we choose

$\alpha_{\text{ox}} = -0.137 \log(L_{2500\text{\AA}}/\text{ergs}^{-1}\text{Hz}^{-1}) + 2.638$ as given by Steffen et al. (2006), then we would have $\langle \log k_{\text{bol}} \rangle = 0.88$ for the SDSS QSOs. Other estimations of the BCs for QSOs at 5100\AA include $k_{\text{bol}} \sim 9$ (Kaspi et al. 2000), $k_{\text{bol}} \sim 10.3 \pm 2.1$ (Richards et al. 2006b), and $k_{\text{bol}} \sim 8.1 \pm 0.4$ (Runnoe et al. 2012), etc., which are roughly consistent with that shown in Figure 2 and suggest that the systematic uncertainties in the BCs should not exceed ± 0.06 dex.

Figure 3 shows the BCs at 5100\AA obtained for the SDSS QSOs in different redshift bins, and these redshift bins are separated by boundaries of 0.3, 0.5, 0.7, 0.9, 1.1, 1.3, 1.5, 1.7, 1.9, 2.4, 2.9, 3.5 and 4.0 (see Kelly & Shen 2013). As seen from Figure 3, the BCs do not depend on $M_{\bullet, \text{vir}}$ in all the redshift bins; and the BCs in different redshift bins spread in roughly the same range, though the mean value of the BCs

z	The BB model				The TLUSTY model				N_Q
	R_S	α	β	$\langle \log \epsilon \rangle$	R_S	α	β	$\langle \log \epsilon \rangle$	
0.3-0.5	0.79	-1.15	0.64	-0.91±0.41	0.72	-1.15	0.56	-0.95±0.38	4,291
0.5-0.7	0.71	-1.25	0.55	-0.93±0.35	0.66	-1.24	0.50	-0.95±0.34	4,205
0.7-0.9	0.62	-1.30	0.47	-0.95±0.30	0.60	-1.32	0.45	-0.98±0.30	3,953
0.9-1.1	0.69	-1.24	0.45	-0.82±0.24	0.70	-1.28	0.45	-0.87±0.24	4,861
1.1-1.3	0.70	-1.26	0.43	-0.82±0.21	0.70	-1.31	0.44	-0.85±0.23	5,865
1.3-1.5	0.69	-1.29	0.43	-0.81±0.20	0.70	-1.36	0.45	-0.85±0.22	5,903
1.5-1.7	0.66	-1.26	0.37	-0.81±0.19	0.71	-1.36	0.43	-0.85±0.21	6,451
1.7-1.9	0.53	-1.14	0.26	-0.81±0.17	0.64	-1.28	0.35	-0.86±0.20	5,840
1.9-2.4	0.22	-1.04	0.15	-0.85±0.18	0.37	-1.15	0.22	-0.87±0.20	7,734
2.4-2.9	0.07	-0.97	0.06	-0.87±0.13	0.25	-1.08	0.13	-0.89±0.14	1,656
2.9-3.5	0.17	-0.99	0.08	-0.88±0.16	0.34	-1.07	0.14	-0.89±0.18	4,176
3.5-4.0	0.17	-1.11	0.08	-0.90±0.15	0.32	-1.07	0.14	-0.90±0.18	1,756

Table 1. Efficiency versus MBH virial mass relation for the SDSS QSOs in different redshift bins. The relationship between ϵ and $M_{\bullet, \text{vir}}$, if any, is fitted by $\log \epsilon = \alpha + \beta \log(M_{\bullet, \text{vir}}/10^8 M_{\odot})$, α and β are the two parameters of the linear fit. The first column is for the redshift range of the QSOs. Symbols R_S and $\langle \log \epsilon \rangle$ represent the Spearman rank correlation coefficient and the mean value of the logarithmic radiative efficiency for the SDSS QSOs in each redshift bin, and N_Q represents the total number of the QSOs in each redshift bin. For the SDSS QSOs in each redshift bin, R_S , α , β , and $\langle \log \epsilon \rangle$ are obtained by adopting either the BB model or the TLUSTY model as listed in the second to fifth columns and the sixth to ninth columns, respectively.

decreases slightly from ~ 9 to ~ 6 with redshift increasing from $z \sim 0.4$ to $z \sim 3.75$. The increasing of the mean value of BCs with redshift is primarily a consequence of that α_{ox} decreases with increasing luminosity and the high redshift QSOs in general have larger luminosities.

3.3 Radiative efficiencies of SDSS QSOs

In this section, we estimate the radiative efficiency for each SDSS QSO in our sample (see section 2). We first estimate the \dot{M}_{acc} for each QSO by matching the observational monochromatic luminosity at 5100Å (or 3000Å, or 1350Å) with both the BB model and the TLUSTY model (see section 3.1). If monochromatic luminosities are available at more than one wavelength, we obtain \dot{M}_{acc} for each monochromatic luminosity and take the mean value of the \dot{M}_{acc} estimates as the accretion rate of the QSO. We also estimate the bolometric luminosity L_{bol} for each QSO by using the empirical method described in section 3.2. With the estimated \dot{M}_{acc} and L_{bol} , the radiative efficiency of a QSO can be then obtained through $\epsilon = L_{\text{bol}}/\dot{M}_{\text{acc}}c^2$.

Figure 4 shows the distribution of the SDSS QSOs in the ϵ - $M_{\bullet, \text{vir}}$ plane, where ϵ is estimated through the BB model. From left to right and top to bottom, each panel shows the results for a given redshift bin, and these redshift bins are separated by boundaries of 0.3, 0.5, 0.7, 0.9, 1.1, 1.3, 1.5, 1.7, 1.9, 2.4, 2.9, 3.5 and 4.0 (see Kelly & Shen 2013). As seen from Figure 4, the radiative efficiencies of the SDSS QSOs appear to be strongly correlated with the masses of the central MBHs in each redshift bin with $z < 1.9$. We perform Spearman's rank order correlation analysis for the QSOs in each redshift bin and the results are listed in Table 1. If adopting the TLUSTY model, we obtain similar results, see Table 1. Apparently, the correlation between ϵ and $M_{\bullet, \text{vir}}$ is strong in the redshift bins with $z \lesssim 1.8$, while it becomes weak at redshift $z \gtrsim 2$. We adopt a power-law form to fit such a correlation, i.e.,

$$\log \epsilon = \alpha + \beta \log \left(\frac{M_{\bullet, \text{vir}}}{10^8 M_{\odot}} \right), \quad (1)$$

where α and β are the two fitting parameters. The parameters that best fit the estimated $\log \epsilon$ versus $\log M_{\bullet, \text{vir}}$ relation in each redshift bin are listed in Table 1. For the lowest redshift bin ($0.3 < z < 0.5$), $\beta = 0.64$ and 0.56 if adopting the BB model and the TLUSTY model, respectively, which is roughly consistent with that obtained in Davis & Laor (2011, $\beta = 0.52$) for the DL QSOs in a similar redshift range. The slight difference might be due to the SED shape adopted here is different from that in the DL sample and the selection criteria for the DL QSO sample is different from that for the SDSS sample. In the first panel ($z = 0.4$), the DL QSOs in Davis & Laor (2011) are also plotted (plus symbols) and apparently the distribution of these DL QSOs are also roughly consistent with the SDSS QSOs. The fitting value of the power-law slope (β) decreases from 0.64 to ~ 0 with increasing redshift from $z \sim 0.2$ to $z \sim 4$ (see Table 1 and Figure 4). For the whole SDSS QSO sample, the best fit gives $\beta = 0.24$, which is substantially smaller than the best fit of $\beta (= 0.64)$ for the lowest redshift bin ($0.3 < z < 0.5$).

Note other studies, e.g., Cao & Li (2008), Wang et al. (2009), Li et al. (2012), and Shankar et al. (2013), in addition to Davis & Laor (2011), also introduced the dependence of the radiative efficiency of QSOs on the MBH mass (and/or redshift), but based on the global integral properties of QSOs through the Sołtan argument (Sołtan 1982; Small & Blandford 1992; Yu & Tremaine 2002).

The left panel of Figure 5 shows the mean value of the logarithmic radiative efficiency of all the SDSS QSOs in each redshift bin, and the right panel of Figure 5 shows that of the SDSS QSOs within a given mass range in each redshift bin. Apparently there is no significant redshift evolution of the mean logarithmic efficiency (e.g., $\langle \log \epsilon \rangle \sim -0.86$ if adopting the BB model, and ~ -0.89 if adopting the TLUSTY model; see Table 1 and Figure 5). The mean value of $\log \epsilon$ obtained through the TLUSTY model is slightly smaller than that obtained through the BB model by ~ 0.03 dex. Consid-

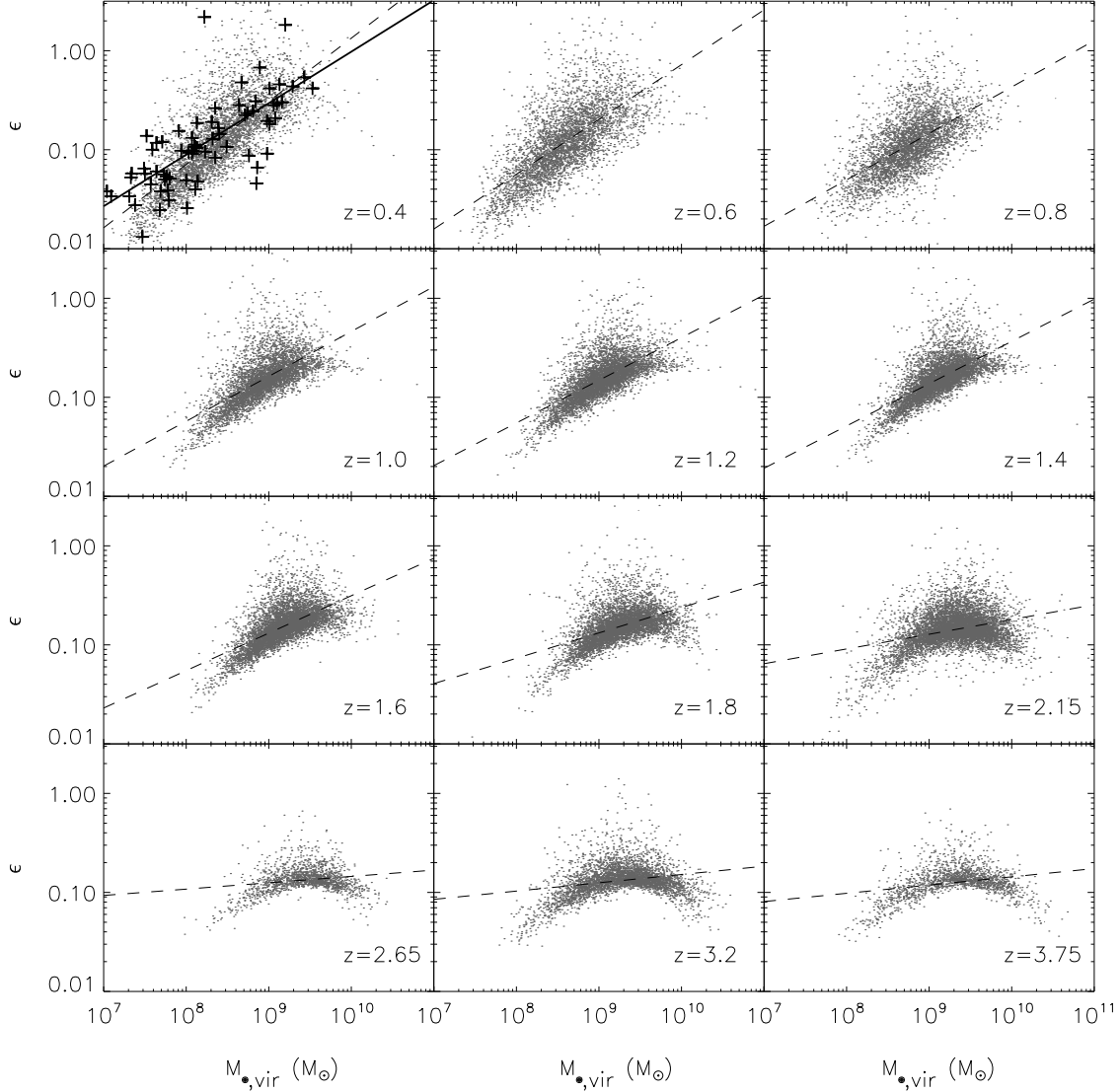


Figure 4. Distributions of the SDSS QSOs in the ϵ – $M_{\bullet,\text{vir}}$ plane. The twelve panels show the results of the radiative efficiency (ϵ) for the SDSS QSOs in different redshift bins, i.e., $0.3 \leq z < 0.5$, $0.5 \leq z < 0.7$, $0.7 \leq z < 0.9$, $0.9 \leq z < 1.1$, $1.1 \leq z < 1.3$, $1.3 \leq z < 1.5$, $1.5 \leq z < 1.7$, $1.7 \leq z < 1.9$, $1.9 \leq z < 2.4$, $2.4 \leq z < 2.9$, $2.9 \leq z < 3.5$, and $3.5 \leq z < 4.0$, respectively. Each grey point represents an SDSS QSO, and each plus symbol represents a QSO in the DL sample estimated by Davis & Laor (2011). The dashed line in each panel represents the best linear fit of the relationship between $\log \epsilon$ and $\log M_{\bullet,\text{vir}}$ in each particular redshift bin. The dependence of ϵ on $M_{\bullet,\text{vir}}$ is strong at redshift $z \lesssim 1.8$ but becomes weak at redshift higher than 2. The solid line represents the fitting for the DL QSOs (Davis & Laor 2011).

ering of the uncertainties in the BC estimations, the mean value of $\log \epsilon$ shown in the left panel of Figure 5 may be overestimated or underestimated at most by ~ 0.06 dex (see discussions in the end of section 3.2), i.e., $\langle \log \epsilon \rangle \sim -0.86 \pm 0.06$ (or $\sim -0.89 \pm 0.06$) by using the BB model (or the TLUSTY model), which corresponds to a mean efficiency of $\sim 0.14 \pm 0.02$ (or $\sim 0.13 \pm 0.02$). Therefore, the mean efficiency of those SDSS QSOs should be in the range of $\simeq 0.11 - 0.16$, which is totally independent of but consistent with those estimations based on the Soltan argument (e.g., Yu & Tremaine 2002; Yu & Lu 2004; Marconi et al.

2004; Yu & Lu 2008; Shankar et al. 2009; Zhang et al. 2012; Shankar et al. 2013). We obtain similar results if alternative using the mean value of ϵ or luminosity-weighted ϵ . In the right panel of Figure 5, we show the mean values of $\log \epsilon$ for those QSOs in each redshift bin with MBH masses in the range of $2.5 \times 10^8 - 4 \times 10^8 M_{\odot}$, $8 \times 10^8 - 1.3 \times 10^9 M_{\odot}$ and $2.5 \times 10^9 - 4 \times 10^9 M_{\odot}$, respectively, which are also roughly consistent with being a constant over the redshift range from 0.3 to 4 (except a seemingly slight increase at $z < 1$ for the QSOs with MBHs in the range of $2.5 \times 10^8 - 4 \times 10^8 M_{\odot}$ and $8 \times 10^8 - 1.3 \times 10^9 M_{\odot}$). It appears that the mean logarith-

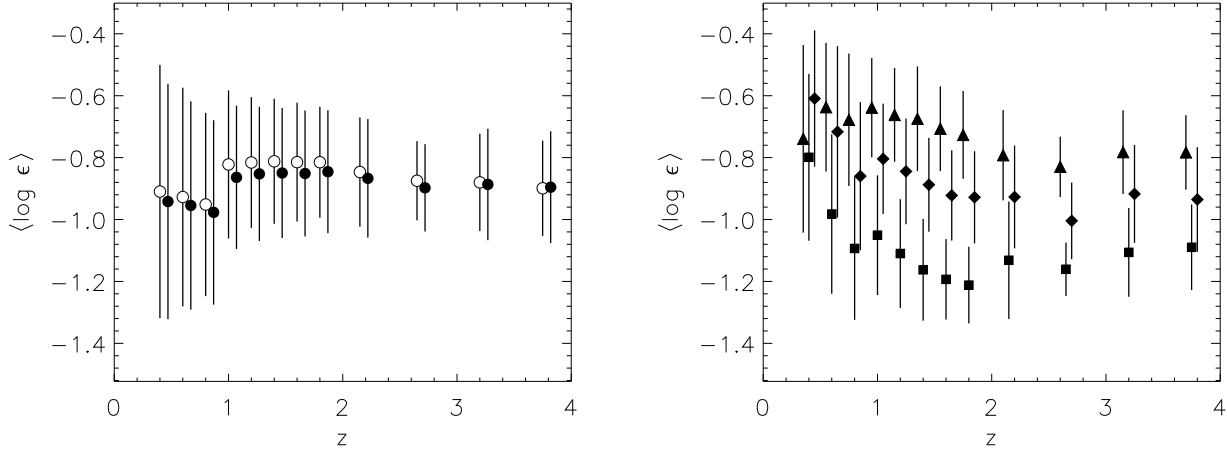


Figure 5. Mean logarithmic radiative efficiency of the type 1 SDSS QSOs in different redshift bins. The left panel shows the mean logarithmic radiative efficiency of all the QSOs in each redshift bin obtained by using either the BB model (open circles) or the TLUSTY model (solid circles). The right panel shows the mean logarithmic radiative efficiency obtained by using the BB model for the QSOs in each redshift bin with MBH masses in the range of $2.5 \times 10^8 - 4 \times 10^8 M_\odot$ (squares), $8 \times 10^8 - 1.3 \times 10^9 M_\odot$ (diamonds) and $2.5 \times 10^9 - 4 \times 10^9 M_\odot$ (triangles), respectively. The bars associated with each symbol represent the standard deviation of the mean value.

mic efficiency for the QSOs with large MBH masses is larger than that with small MBH masses (right panel of Figure 5). However, this tendency seems to be mainly caused by the selection effects but not intrinsic (as seen also from Figure 4 and discussions in section 4).

The apparent strong dependence of ϵ on $M_{\bullet, \text{vir}}$ shown in Figure 4 appears to suggest that more massive MBHs statistically rotate faster than less massive MBHs in QSOs, as discussed in Davis & Laor (2011). However, it is possible that this apparent correlation is only a result of the selection effects of the SDSS QSO sample and the biases induced by various assumptions in the estimations of ϵ , and the intrinsic radiative efficiency of individual SDSS QSOs may be not correlated with the MBH true mass (Raimundo et al. 2012, but Davis & Laor 2011; Laor & Davis 2011). To investigate whether the above $\epsilon - M_{\bullet, \text{vir}}$ correlation is intrinsic or not, the key is in understanding the selection effects and the various biases involved in the ϵ estimations, which will be studied in details in the following section 4.

3.4 Eddington ratios of SDSS QSOs

Figure 6 shows the distribution of the SDSS QSOs in the Eddington ratio (f_{Edd}) versus the MBH virial mass ($M_{\bullet, \text{vir}}$) plane, where $f_{\text{Edd}} = L_{\text{bol}}/L_{\text{Edd}}(M_{\bullet, \text{vir}})$ and $L_{\text{Edd}}(M_{\bullet, \text{vir}}) \sim 1.3 \times 10^{46} \text{ erg s}^{-1} (M_{\bullet, \text{vir}}/10^8 M_\odot)$. As seen from Figure 6, the Eddington ratio is strongly anti-correlated with the MBH virial mass for the SDSS QSOs in every redshift bin, similar to that found by Davis & Laor (2011, see Figure 13 therein) for 80 PG QSOs at low redshift ($z \leq 0.5$). Generally the larger the MBH virial mass, the smaller the Eddington ratio. However, one should note that the obtained distribution of the Eddington ratios in the $f_{\text{Edd}} - M_{\bullet, \text{vir}}$ plane is also affected by the selection effects and the biases induced by the usage of the MBH virial mass (but not the MBH true mass). Similar to that shown for the radiative efficiency in Figures 9 and 10 in section 4, the correlation between Eddington ratio

and MBH virial mass can also be explained by the selection effects and the biases induced by the usage of the MBH virial masses. In this study, we do not intend to expand the discussion on Eddington ratios as that done for radiative efficiencies in section 4.

4 BIASES AND SELECTION EFFECTS IN THE RADIATIVE EFFICIENCY ESTIMATIONS

4.1 Uncertainties in the \dot{M}_{acc} estimations

The above estimations of \dot{M}_{acc} may be not accurate as (1) the adopted virial masses of MBHs deviate from the true masses; (2) the MBH spins and inclination angles are assumed to be fixed values but in reality they are probably not; and (3) the accretion disk model(s) may be oversimplified. Figure 7 illustrates the uncertainties in the \dot{M}_{acc} estimations induced by these various factors as detailed below.

First, the uncertainty due to the usage of the virial mass as the true MBH mass. The estimated virial masses of MBHs may deviate from the true masses with a scatter of 0.3 – 0.4 dex (e.g., Shen et al. 2008, 2011). We perform following calculations to quantify the uncertainty of the \dot{M}_{acc} estimation induced by the usage of the virial mass (rather than the true MBH mass). Assuming a typical QSO, of which the true MBH mass is $M_{\bullet, \text{t}} = 10^8 M_\odot$ and spin is $a = 0.67$, accreting material via a true rate of $\dot{M}_{\text{acc}, \text{t}} = 0.67 M_\odot \text{ yr}^{-1}$ (corresponding to an Eddington ratio of 0.3), and the inclination angle of the disk to the line of sight is $i = \arccos(0.8)$. The optical band luminosity at 5100Å of this system is predicted to be $L_{5100\text{Å}} = 10^{44.56} \text{ erg s}^{-1}$ by adopting the BB model. Assuming a virial mass of the MBH $M_{\bullet, \text{vir}}$, scattered around $M_{\bullet, \text{t}}$, we may estimate the accretion rate \dot{M}_{acc} according to $L_{5100\text{Å}}$ and $M_{\bullet, \text{vir}}$ through the procedures described in section 3.1. For this specific case, 5100Å, 3000Å and 1350Å are all at the left side of the turnover of the disk emission spectrum (which is also true

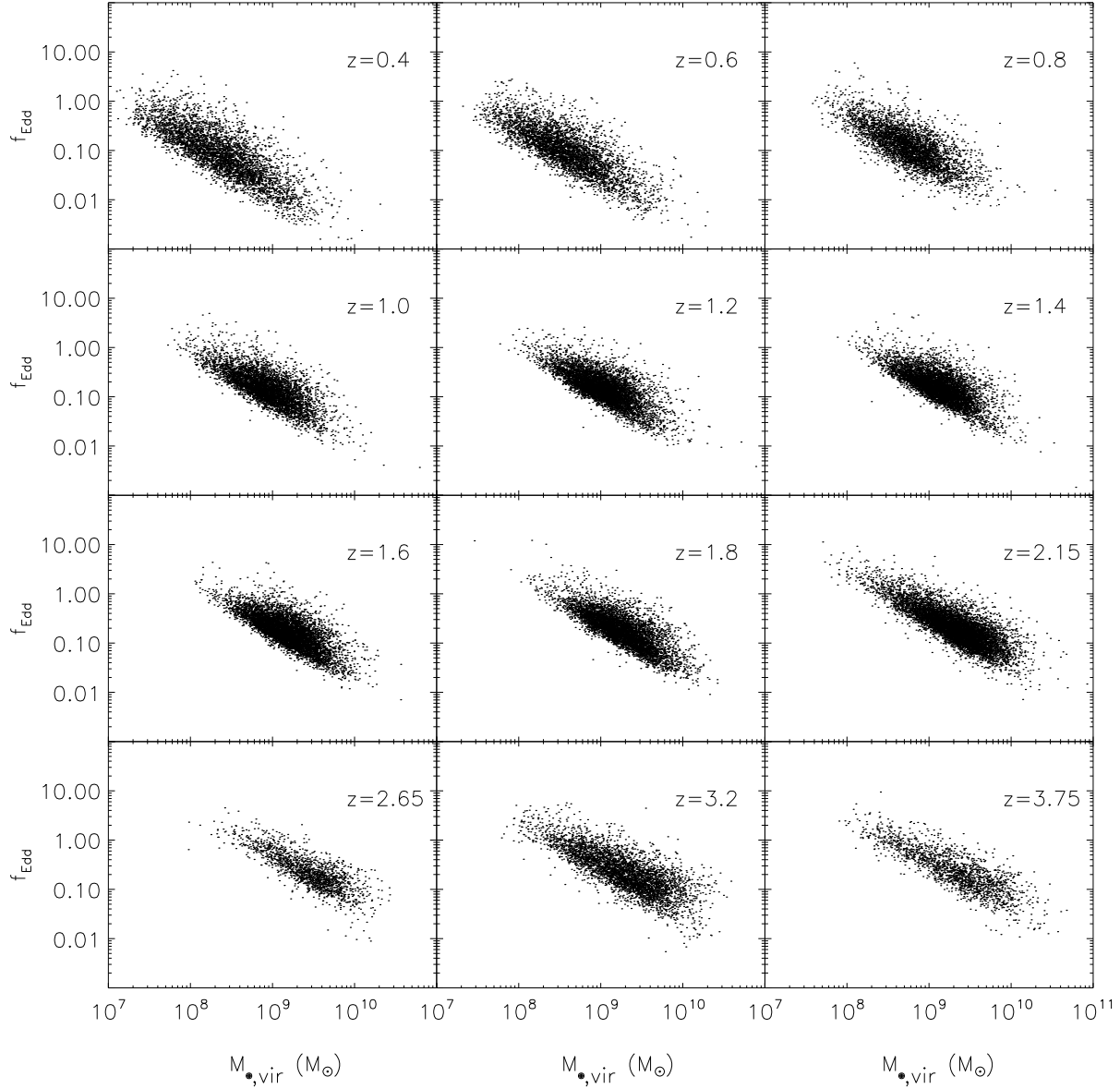


Figure 6. Distributions of the SDSS QSOs in the $f_{\text{Edd}} - M_{*,\text{vir}}$ plane at different redshift bins. Each grey point represents an SDSS QSO.

for more than 90% of the type 1 SDSS QSOs). Clearly, \dot{M}_{acc} can be underestimated (or overestimated) by adopting the BB model if $M_{*,\text{vir}}$ is larger (or smaller) than $M_{*,\text{t}}$ (see the blue circles in the left panel of Figure 7). For a typical deviation of $M_{*,\text{vir}}$ from $M_{*,\text{t}}$, i.e., 0.3 dex, \dot{M}_{acc} may be either underestimated or overestimated by a factor of ~ 2 . If alternatively adopting the TLUSTY model for the same system, we have $L_{5100\text{\AA}} = 10^{44.51} \text{erg s}^{-1}$. Similarly we can obtain the best fit of \dot{M}_{acc} for each set of $(L_{5100\text{\AA}}, M_{*,\text{vir}})$, as represented by the red triangles in the left panel of Figure 7. In these cases, the uncertainties in the estimated \dot{M}_{acc} are similar to that by the BB model above. For an observational sample of QSOs, the virial masses of the QSO central MBHs

are more likely to be overestimated (or underestimated) at the high (or low) mass end, which may consequently leads to the overestimate (or underestimate) of the radiative efficiencies and thus could contribute to the apparent correlation found in section 3 (see also the discussions in Davis & Laor 2011). However, we note here that the turnover of the disk emission spectra may move to the left side of 1350\AA for some QSOs with extreme large MBH masses ($\gtrsim 10^{10} M_{\odot}$) and small Eddington ratios ($\lesssim 0.04$). For these rare cases, if the virial masses of the QSO central MBHs are overestimated, the radiative efficiencies may be consequently underestimated, which is totally different from that for QSOs with smaller MBH masses and high Eddington ratios.

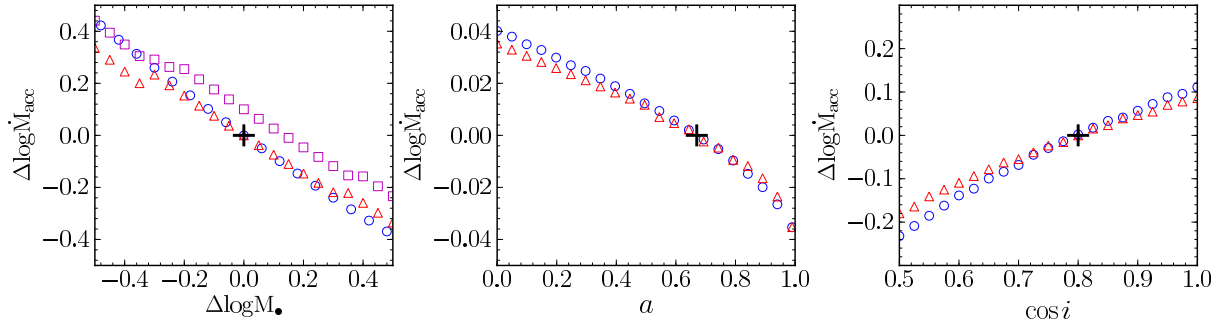


Figure 7. Uncertainties in the accretion rate estimations ($\Delta \log \dot{M}_{\text{acc}} = \log \dot{M}_{\text{acc}} - \log \dot{M}_{\text{acc,t}}$) for QSOs with the same intrinsic parameters $M_{\bullet,t} = 10^8 M_{\odot}$, $a = 0.67$, $\dot{M}_{\text{acc,t}} = 0.67 M_{\odot} \text{yr}^{-1}$, $\cos i = 0.8$ (marked by the black plus symbol in each panel). Left, middle and right panels show the uncertainties in the \dot{M}_{acc} estimations solely induced by the deviation of the virial mass from the true MBH mass ($\Delta \log M_{\bullet} = \log M_{\bullet,\text{vir}} - \log M_{\bullet,t}$), the set of a fixed value for the MBH spin (a), and the set of a fixed value of the inclination angle (i), respectively. In each panel, blue circles and red triangles show the uncertainties in the \dot{M}_{acc} estimations by adopting the BB model and the TLUSTY model, respectively. In the left panel, \dot{M}_{acc} is obtained by assuming that a and i are the same as the intrinsic ones while $M_{\bullet,\text{vir}}$ is different from $M_{\bullet,t}$. Magenta squares represent the uncertainties in the \dot{M}_{acc} estimations obtained from the fitting by adopting the TLUSTY model, however, the $L_{5100\text{\AA}}$ value, which is used for the model fitting, is generated by the BB model. In the middle panel, \dot{M}_{acc} is obtained by assuming that $M_{\bullet,\text{vir}}$ and i are the same as the intrinsic ones while a is set to be different from the intrinsic value. In the right panel, \dot{M}_{acc} is obtained by assuming that $M_{\bullet,\text{vir}}$ and a are the same as the intrinsic ones while i is set to be different from the intrinsic value.

Second, the uncertainties due to the usage of a fixed value of a and a fixed value of i . We first assume that the true MBH mass $M_{\bullet,t}$ and inclination angle i of the systems are known and arbitrarily adopt a value of a to do the fitting in order to check the uncertainty solely due to the set of a fixed a (different from the intrinsic value). We find that the best-fit of \dot{M}_{acc} only deviates slightly, at most 0.04 dex or 10%, from its true value (see the middle panel of Figure 7). The reason is that $L_{5100\text{\AA}}$ is insensitive to the MBH spin at $M_{\bullet,t} \lesssim 10^8 M_{\odot}$ in the thin accretion disk model(s) for QSOs. If choosing larger $M_{\bullet,t}$ (e.g., $\gtrsim 10^9 M_{\odot}$), the uncertainty introduced to the estimate of \dot{M}_{acc} is no more than 50% by an arbitrary set of a (see also Davis & Laor 2011). Most SDSS QSOs are type 1 QSOs, their inclination angles i may be uniformly distributed in $\cos i$ between 0.5 and 1. We now assume that the true MBH mass $M_{\bullet,t}$ and spin a of the systems are known and obtain the best fit values of \dot{M}_{acc} by arbitrarily setting the value of i . The uncertainty induced by the set of a fixed value for i ($\cos i$) is shown in the right panel of Figure 7, which are at most 0.2 dex. In this section, we set a fixed value of $i = \arccos(0.8)$ for the fitting, with which the results obtained here can be directly compared with that found in Davis & Laor (2011) and Raimundo et al. (2012).

Third, the uncertainty induced by the choice of a specific accretion disk model. The real accretion process may be not accurately reflected by either the BB model or the TLUSTY model. Adopting a specific disk model may then introduce some (systematic) bias to the accretion rate estimations. To illustrate this uncertainty, we first generate a number of QSOs with optical luminosity predicted by the TLUSTY (or BB) model, but then adopt the BB (or TLUSTY) model to estimate \dot{M}_{acc} by using $L_{5100\text{\AA}}$ and $M_{\bullet,\text{vir}}$. We find that the estimated \dot{M}_{acc} could be systematically under-estimated or (over-estimated) due to the choice of an accretion disk model that not exactly reflect the underlying true disk accretion physics (for example, see the magenta squares shown in the left panel of Figure 7).

We further perform Monte-Carlo calculations to illus-

trate the uncertainties in the accretion rate estimations due to the above factors. We first generate mock QSO samples in which all QSOs have the same intrinsic properties ($M_{\bullet,t} = 10^8 M_{\odot}$ and $\dot{M}_{\text{acc}} = 0.67 M_{\odot} \text{yr}^{-1}$). The spin and inclination angle are set to be $a = 0.67$ and $i = \arccos(0.8)$, respectively, for all the QSOs in the first sample; while $i = \arccos(0.8)$ and a is set to be uniformly distributed in the range from 0 to 0.99 for the QSOs in the second sample; and $a = 0.67$ and i is assumed to be uniformly distributed in $\cos i$ between 0.5 and 1 for the QSOs in the third sample. We randomly assign $M_{\bullet,\text{vir}}$ to each mock QSO in the first sample according to a Gaussian distribution around $M_{\bullet,t}$ with a scatter of 0.3 dex. We obtain $L_{5100\text{\AA}}$ by both the BB model and the TLUSTY model for each QSO, respectively. We obtain three samples of QSOs with given observational properties of $L_{5100\text{\AA}}$ and $M_{\bullet,\text{vir}}$ (or $M_{\bullet,t}$). We adopt the procedures described in section 3.1 to estimate \dot{M}_{acc} for these mock QSOs. Figure 8 shows the probability distribution of $\Delta \log \dot{M}_{\text{acc}} = \log \dot{M}_{\text{acc}} - \log \dot{M}_{\text{acc,t}}$ for the first (left panel), second (middle panel) and third sample (right panel), respectively. In each panel, the solid and dashed lines show the results obtained by adopting the BB model and the TLUSTY model, respectively. In the left panel, \dot{M}_{acc} are obtained for each QSO in the first sample by assuming $a = 0.67$, $\cos i = 0.8$, and the virial mass as the “true” MBH mass; in the middle and right panel, \dot{M}_{acc} is obtained for each QSO in the second and third samples by assuming $M_{\bullet,\text{vir}} = M_{\bullet,t}$, $\cos i = 0.8$ and $a = 0.67$. Figure 8 clearly illustrates that the uncertainties of the \dot{M}_{acc} estimations induced by the deviations of the virial masses of MBHs from the true masses could be as large as a factor of 2 and can have significant effects on the ϵ estimations, while the errors due to inaccurate settings of a , i and the choice of the disk model are relatively less significant. If alternatively choosing other values of $M_{\bullet,t}$ and \dot{M}_{acc} , we obtain similar results as that shown in Figure 8.

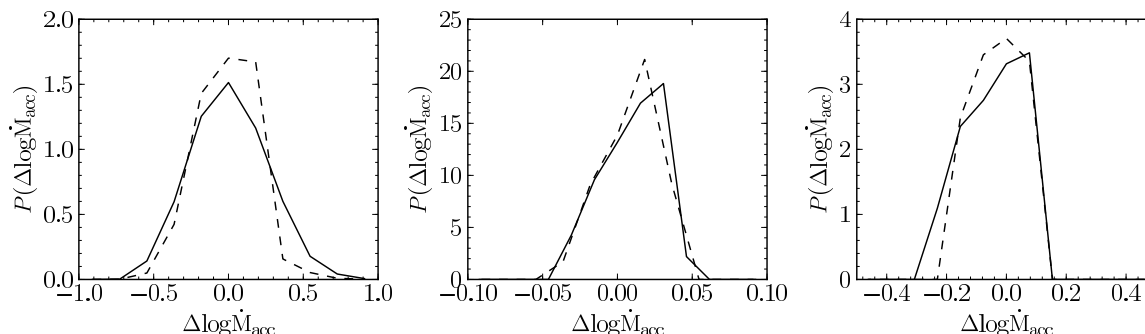


Figure 8. Probability distributions of $\Delta \log \dot{M}_{\text{acc}} = \log \dot{M}_{\text{acc}} - \log \dot{M}_{\text{acc,t}}$ obtained from the mock QSO samples by adopting different assumptions in the fitting. The first mock sample is generated by assuming all QSOs have the same intrinsic properties ($M_{\bullet,t} = 10^8 M_{\odot}$, $a = 0.67$ and $\dot{M}_{\text{acc,t}} = 0.67 M_{\odot} \text{yr}^{-1}$ and $i = \text{acos}(0.8)$). The QSOs in the second and third mock samples have the same intrinsic properties as that in the first mock sample, except that a is assumed to be distributed uniformly in the range from 0 to 0.99 and i is assumed to be uniformly distributed in $\cos i$ between 0.5 and 1, respectively. The virial mass is randomly assigned to each mock QSO in the first sample according to a Gaussian distribution with a mean of $M_{\bullet,t}$ and a scatter of 0.3 dex. Left panel shows the resulted distribution from the estimations of \dot{M}_{acc} for the first mock sample by assuming that the virial mass is the “true” MBH mass, $a = 0.67$, and $i = \text{acos}(0.8)$. Middle and right panels show the resulted distributions for the second sample and the third sample, respectively, by assuming $M_{\bullet} = M_{\bullet,t}$, $a = 0.67$ and $i = \text{acos}(0.8)$. In each panel, the solid and dashed lines represent the results obtained by adopting the BB model and the TLUSTY model, respectively.

4.2 Monte-Carlo simulations

In this section, we investigate whether the correlation between radiative efficiency and MBH mass is intrinsic or simply due to various biases in the accretion rate estimations and/or the selection effects of the SDSS QSO sample (mainly a flux limit sample).

First, we generate mock SDSS QSOs based on the true mass function of MBHs (BHMF, $\Phi(M_{\bullet})$) and the true Eddington ratio (f_{Edd}) distribution function (ERDF, $\Phi(f_{\text{Edd}})$) obtained by Kelly & Shen (2013, see their Tables 1 and 2). According to the BHMF and the ERDF at each redshift bin, we randomly assign the MBH mass $M_{\bullet,t}$ (in the range from $10^6 M_{\odot} - 10^{11} M_{\odot}$) and the Eddington ratio f_{Edd} (in the range from 10^{-4} to 10^1) to each mock QSO. Kelly & Shen (2013) argued that the Eddington ratio distribution may be independent of the MBH mass and the difference in the Eddington ratio distribution for MBHs with different masses at $0.8 < z < 2.65$ might be only an effect of the uncertainties in the MBH mass estimations by the usage of the CIV lines. We assume that the Eddington distribution is the same for MBHs with different masses. Assuming that ϵ_t is randomly distributed over the range from 0.057 to 0.31, corresponding to a spin range from 0 to 0.998,³ the intrinsic accretion rate is then $\dot{M}_{\text{acc,t}} = f_{\text{Edd}} L_{\text{Edd}} / \epsilon_t c^2$. The inclination angle i is assumed to be uniformly distributed in $\cos i$ from 0.5 to 1. Given the intrinsic parameters of each mock QSO, i.e., $M_{\bullet,t}$, a , $\dot{M}_{\text{acc,t}}$ and i , the optical band luminosity $L_{5100\text{\AA}}$ can be obtained by adopting the BB (or TLUSTY) model. A virial mass of the central MBH in each mock QSO is assigned according to a Gaussian distribution with a mean of $\log M_{\bullet,t}$ and a scatter of 0.3 dex. With the above procedure, we generate 5×10^6 mock QSOs in each redshift bin, and

finally we have a large number of mock QSOs that have not only the “observational measurements” of their virial mass $M_{\bullet,\text{vir}}$ and the optical band luminosity(/-ies) $L_{5100\text{\AA}}$ (and/or $L_{3000\text{\AA}}$, and/or $L_{1350\text{\AA}}$) but also known intrinsic properties of $M_{\bullet,t}$, \dot{M}_{acc} and ϵ . The optical band luminosities are produced at 5100Å for those QSOs with $z < 0.35$, at 5100Å and 3000Å for those QSOs with $0.35 < z < 0.9$, at 3000Å for those QSOs with $0.9 < z < 1.5$, at 3000Å and 1350Å with $1.5 < z < 2.25$, and at 1350Å for those QSOs with $2.25 < z < 4$, respectively, in order to mimic the SDSS QSO sample. We take these mock QSOs as the parent populations of the QSOs in each redshift bin that can be detected by a survey like the SDSS.

With the “observational” properties of the mock QSOs, i.e., $M_{\bullet,\text{vir}}$ and $L_{5100\text{\AA}}$ (and/or $L_{3000\text{\AA}}$, and/or $L_{1350\text{\AA}}$), we can adopt the same procedure as that described in section 3 to estimate ϵ . In order to single out the effects on the ϵ estimations due to the deviation of $M_{\bullet,\text{vir}}$ from $M_{\bullet,t}$, we also estimate ϵ for the mock QSOs by using their optical luminosity $L_{5100\text{\AA}}$ (and/or $L_{3000\text{\AA}}$, and/or $L_{1350\text{\AA}}$) and the true MBH mass $M_{\bullet,t}$. We further consider the selection criteria for those mock QSOs similar to that for the SDSS QSOs, i.e., only those mock QSOs with apparent i -band magnitude ≤ 19.1 at $z \leq 2.9$ and ≤ 20.2 at $z > 2.9$ can be taken as the mock SDSS QSOs (see section 2). To select mock SDSS QSOs, we first convert $L_{5100\text{\AA}}$ (or $L_{3000\text{\AA}}$, or $L_{1350\text{\AA}}$) to the monochromatic luminosity at i -band (7471Å) by assuming a power law spectrum with a canonical slope of $\alpha_{\text{opt}} = -0.5$, and then use the K -correction, including the effects of both the continuum and the emission lines, given by Richards et al. (2006b) to calculate the apparent i -band magnitude of each mock QSO. Here we adopt $\alpha_{\text{opt}} = -0.5$ because the K -corrections given by Richards et al. (2006b) are obtained by using a canonical slope of -0.5 . Finally, we obtain the mock SDSS QSOs according to the above selection criteria, which consist of a small fraction ($\sim 1 - 5\%$) of the parent mock sample at each redshift bin. Here we adopt the standard Λ CDM cosmology

³ If alternatively assuming that the radiative efficiencies for all QSOs are the same, i.e., $\epsilon_t = 0.13$ (similar to the mean efficiency shown in Figure 3; or 0.1 or 0.2), corresponding to a spin $a \sim 0.83$ (or ~ 0.67 or 0.96), we find little changes of our following conclusions.

with $(H_0, \Omega_M, \Omega_\Lambda) = (71 \text{ km s}^{-1} \text{ Mpc}^{-1}, 0.27, 0.73)$. Similar to that in section 3, we do the simulations by adopting both the BB model and the TLUSTY model, and we find that the results obtained from two different models are similar. For simplicity, only the results obtained by adopting the BB model are presented below in this section.

Figure 9 shows the normalised probability density distribution of the mock QSOs on the $\log \epsilon - M_{\bullet, \text{vir}}$ (or $\log \epsilon - M_{\bullet, t}$) plane. Without considering the selection effects, the radiative efficiencies ϵ of the mock QSOs estimated from $L_{5100\text{\AA}}$ and $M_{\bullet, t}$ appear to be independent of $M_{\bullet, t}$ (see the red contour lines in each redshift bin). By performing Spearman's rank correlation analysis, we do not find any strong correlations between ϵ and $M_{\bullet, t}$ for the whole mock sample (without considering the selection effects). The estimated ϵ scatter around the mean of the input values ~ 0.18 mainly because the BC is randomly assigned to each mock QSO according to the empirical SED of QSOs as described in section 3.2.⁴ For the mock SDSS QSOs, there is an obvious strong correlation between the radiative efficiencies ϵ (estimated from $L_{5100\text{\AA}}$ and $M_{\bullet, t}$) and the true MBH mass $M_{\bullet, t}$ (see the black contour lines in each panel of Figure 9). Similar to that for the SDSS QSOs, we adopt a power law form to fit these correlations, i.e., $\epsilon \propto M_{\bullet, t}^\beta$, and find $\beta = 0.46, 0.50, 0.51, 0.56, 0.57, 0.56, 0.48, 0.57, 0.63, 0.60, 0.45$ and 0.36 for the redshift bins from low to high, respectively. Further considering the deviation of $M_{\bullet, \text{vir}}$ from $M_{\bullet, t}$, we find that the radiative efficiency ϵ (estimated from $L_{5100\text{\AA}}$ and $M_{\bullet, \text{vir}}$) are strongly correlated with $M_{\bullet, \text{vir}}$ (see the filled color contours in Figure 9). Adopting the same power-law form to fit these correlations, i.e., $\epsilon \propto M_{\bullet, \text{vir}}^\beta$, we find $\beta = 0.54, 0.60, 0.60, 0.67, 0.68, 0.69, 0.33, 0.48, 0.56, 0.52, 0.37$ and 0.28 for the redshift bins from low to high, respectively. It appears that the slope β is larger at low redshift ($z \lesssim 1.8$) and smaller at high redshift ($z \gtrsim 2$), compared with the cases without considering the deviation of $M_{\bullet, \text{vir}}$ from $M_{\bullet, t}$, which is mainly due to the biases induced by the deviations of the virial masses from the true MBH masses. Similar to that for the SDSS QSOs, the slope β is relatively large at low redshift and small at high redshift.

Figure 10 shows the comparison of the normalised probability density distributions of the mock SDSS QSOs with that of the SDSS QSOs in the $\log \epsilon - M_{\bullet, \text{vir}}$ plane. Apparently, the distributions of the mock SDSS QSOs in the $\log \epsilon - \log M_{\bullet, \text{vir}}$ plane are roughly consistent with that of the SDSS QSOs in all the redshift bins. According to Figures 9 and 10, it is clear that the selection effects can be the dominant factors that cause the strong correlation between ϵ and $M_{\bullet, \text{vir}}$, and the usage of the virial mass $M_{\bullet, \text{vir}}$ as the true MBH mass also contribute some to the correlation but it is

less significant comparing with the selection effects. As discussed in section 4.1, the uncertainties in the ϵ estimations induced by the usage of a constant inclination angle i play little role in generating the $\epsilon - M_{\bullet, \text{vir}}$ correlation.

The simplest explanation for the arouse of an apparent correlation between ϵ and $M_{\bullet, \text{vir}}$, as an addition to the above Monte-Carlo analysis, is as follows. In the standard thin accretion disk scenario, the accretion rate is related to the optical luminosity as $\dot{M}_{\text{acc}} \propto L_{\text{opt}}^{3/2} M_{\bullet}^{-1}$ according to Davis & Laor (2011). Since $L_{\text{bol}} \propto L_{\text{opt}}$, $\epsilon = L_{\text{bol}} / \dot{M}_{\text{acc}} c^2 \propto L_{\text{opt}}^{-1/2} M_{\bullet}$. For a given M_{\bullet} , the larger the efficiency, the smaller the optical luminosity L_{opt} and thus the larger the probability that the QSO is missed in a flux limited sample. The smaller the MBH mass, the larger the probability that QSOs with high radiative efficiencies can be detected by a flux limited survey like SDSS. For high redshift bins ($z \gtrsim 2.15$), the general tendency of increasing efficiency with increasing MBH mass is similar to that for low redshift bins if the MBH mass is smaller than a few times $10^9 M_{\odot}$; while it turns over if the MBH mass is larger. For the QSOs with MBH masses larger than a few times $10^9 M_{\odot}$ at high redshift $z \gtrsim 2.25$, the observational measurement is only provided at 1350\AA , which is probably at the right side of the disk emission spectrum. For these cases, the empirical SEDs adopted in this study, a monotonically increasing function at $1\mu\text{m} - 1300\text{\AA}$, are somewhat different from the disk emission spectra, which might lead to underestimation of the bolometric luminosities and thus underestimation of the radiative efficiencies. This could be part of the reason that the estimated radiative efficiencies of many QSOs with MBH mass $\gtrsim 10^{10} M_{\odot}$ at high redshift bins ($z \gtrsim 2.15$) deviate from the correlation between efficiency and MBH mass at lower redshift. Furthermore, the accretion rate could be overestimated by using the monochromatic luminosity $L_{1350\text{\AA}}$ if the MBH virial mass is an overestimate of the true MBH mass (probably true for many QSOs at the high mass end at high redshift, e.g., $z \gtrsim 2.25$) since the turnover of the disk emission spectra may move to the left side of 1350\AA for some QSOs with extreme large MBH mass ($\gtrsim 10^{10} M_{\odot}$) and small Eddington ratio ($\lesssim 0.04$; see discussion in section 4.1). Such a behavior is quite different from that for the cases with lower MBH masses and higher Eddington ratios. The turnover of the trend for the QSO radiative efficiencies in high redshift bins ($z \gtrsim 2.15$) at high mass end can also be partly explained by this.

One may note, however, that the probability distributions of the mock SDSS QSOs in the $\log \epsilon - \log M_{\bullet, \text{vir}}$ plane seem to be offset from that of the SDSS QSOs. The slopes β of the best fits are also not exactly the same as that of the SDSS QSOs. Especially in the high redshift bins ($z \gtrsim 2$), the $\epsilon - M_{\bullet, \text{vir}}$ correlation obtained from the mock QSOs is still significant, while that obtained from the SDSS QSOs is very weak. The above differences between the mock SDSS QSOs and the SDSS QSOs might be not a surprise as a number of complications are not considered in the above ϵ estimations for both the SDSS QSOs and the mock QSOs. First, we do not consider the contamination by the host galaxy light and the dust extinction for each individual SDSS QSO, which may introduce errors to both the \dot{M}_{acc} and L_{bol} estimations and consequently the ϵ estimations for the SDSS QSOs (see also Raimundo et al. 2012). Second, the bolomet-

⁴ The contours center seem to be not exactly the mean value (0.18) of the input efficiencies for some redshift bins mainly because of the following reason. The efficiency for each QSO is estimated by using the bolometric luminosity obtained empirically and the accretion rates obtained by adopting the standard thin disk model. This method is not completely self-consistent, i.e., the efficiency estimate could be slightly offset from the input intrinsic efficiency for the standard thin disk model if the empirical SED is not exactly the same as the SED predicted by the standard thin disk model, which is a caveat of both our model and other previous models (e.g., Davis & Laor 2011).

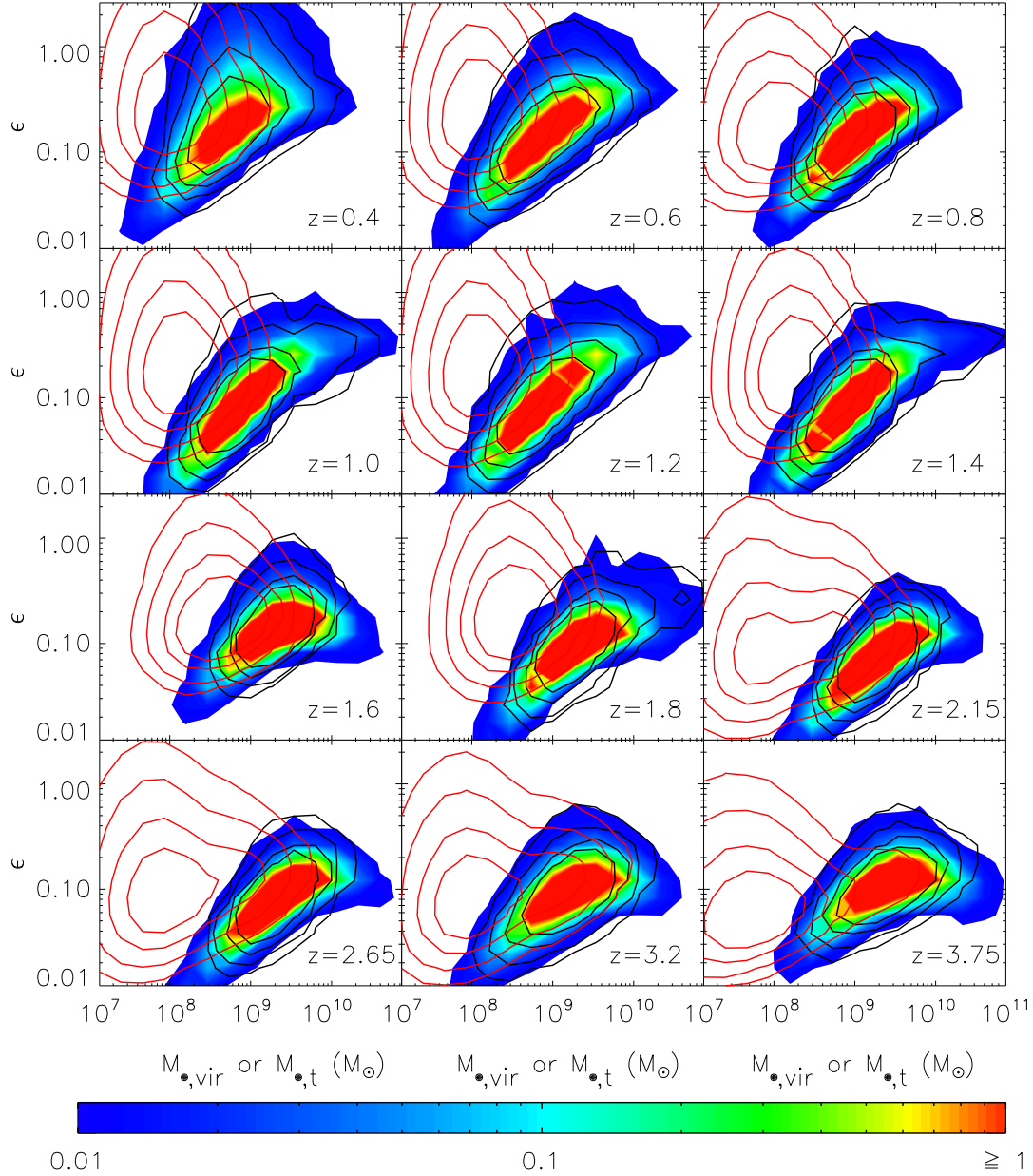


Figure 9. Probability density distributions of the mock QSOs at different redshift bins in the $\log \epsilon - M_{\bullet, \text{vir}}$ (or $\log \epsilon - M_{\bullet, t}$) plane. In each redshift bin, the red contour lines represent the probability density distribution of all the mock QSOs without considering the selection effect, and the radiative efficiency ϵ of each mock QSO is estimated by using $(L_{5100\text{\AA}}, M_{\bullet, t})$; the black contour lines represent the distribution of those mock QSOs that satisfy the selection criteria as that for the SDSS QSOs, and the radiative efficiency ϵ of each mock QSO is estimated by using $(L_{5100\text{\AA}}, M_{\bullet, t})$; and the filled color contours represent the distribution of those mock QSOs that satisfy the selection criteria as that for the SDSS QSOs, and the radiative efficiency ϵ of each mock QSO is estimated by using $(L_{5100\text{\AA}}, M_{\bullet, \text{vir}})$. The probability densities represented by the four contour lines (both in black and in red) from the outer to inner regions are 0.01, 0.05, 0.2 and 0.5, respectively, in units of per $\log M_{\bullet, \text{vir}}$ (or $\log M_{\bullet, t}$) per $\log \epsilon$. The bar at the bottom shows the scales of the filled color contours.

ric luminosity L_{bol} is obtained according to the empirical SED of QSOs and its associated scatters, which are obtained from the multi-wavelength observations of samples with a small number of QSOs that only cover limited ranges of luminosity and redshift (see section 3.2). The usage of this SED may introduce not only scatters but also systematic biases in the ϵ estimations. The small spread in the shapes

of the adopted empirical SEDs may be also important for the resulted statistics of the ϵ estimations, as pointed out by Laor & Davis (2011). Third, the mock QSOs are generated according to the true BHMF and ERDF given by Kelly & Shen (2013). In Kelly & Shen (2013), the obtained BHMF and ERDF can best fit the QSO observations, however, they are obtained by assuming a constant bolometric

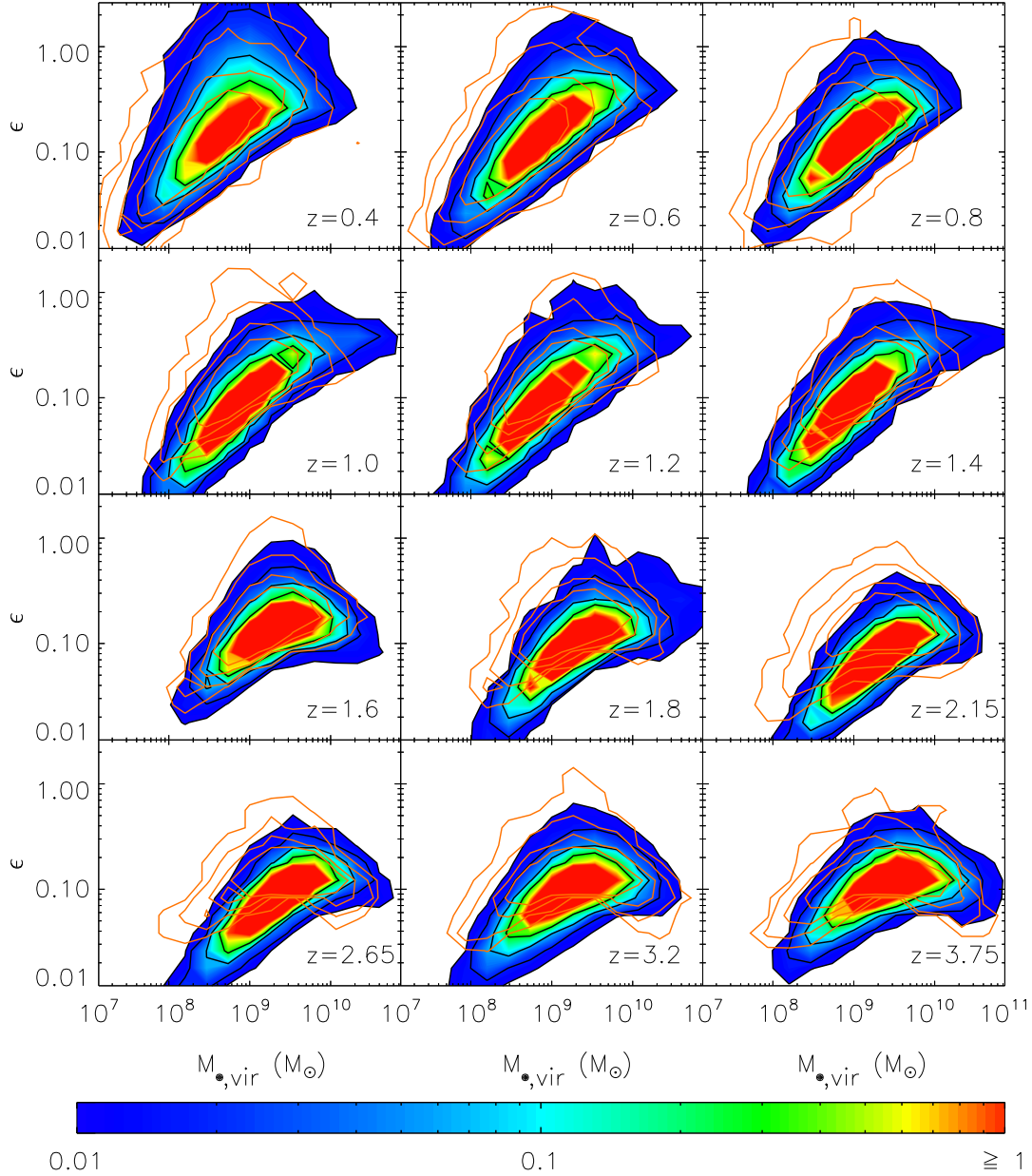


Figure 10. Probability density distributions of the mock SDSS QSOs and the SDSS QSOs in the $\log \epsilon - \log M_{\bullet, \text{vir}}$ plane. The filled color contours (and also the black contour lines) represent the distribution of the mock SDSS QSOs (the same as the filled color contours in Figure 9) and the orange contour lines represent the distribution of the SDSS QSOs in each redshift bin. The SDSS QSOs here correspond to the observational SDSS QSO sample (see section 2 and Figure 4). The probability densities represented by the four contour lines (both in black and in orange) from the outer to inner regions are 0.01, 0.05, 0.2 and 0.5, respectively, in units of per $\log M_{\bullet, \text{vir}}$ per $\log \epsilon$. The bar at the bottom shows the scales of the filled color contours.

correction. Since the BCs of the type 1 QSOs may have a large scatter and may also depend on the Eddington ratio and the true MBH mass (e.g., Vasudevan & Fabian 2007, 2009; Lusso et al. 2010; Jin et al. 2012), the BHMF and ERDF obtained by Kelly & Shen (2013) may still deviate somewhat from the true distributions, which may further introduce some uncertainties in the distributions of the mock SDSS QSOs in the $\log \epsilon - \log M_{\bullet, \text{vir}}$ plane. One needs to self-consistently consider all the factors, including the BHMF,

ERDF, BCs and the radiative efficiencies, etc., simultaneously, to fully solve this problem.

In principle, one could also check whether an intrinsic correlation between ϵ_t and $M_{\bullet, t}$ can be ruled out (or confirmed) by comparing the results obtained from the SDSS QSOs with that obtained from mock SDSS QSO samples. To check this, we re-generate the mock SDSS QSO sample by assuming that $\epsilon_t = 0.1(M_{\bullet, t}/10^8 M_{\odot})^{0.5}$, as an alternative to the initial setting of a random ϵ_t in the above calcula-

tions. According to this new mock SDSS QSO sample, we find that the resulted correlation between ϵ and $M_{\bullet, \text{vir}}$ is generally steeper than that obtained above by assuming a constant ϵ_t in each redshift bin. For example, $\beta = 0.56, 0.62$, and 0.75 for the first three redshift bins, respectively. The differences in β may help to distinguish whether there is indeed an intrinsic correlation between ϵ_t and $M_{\bullet, t}$. Because of the various complications and large uncertainties in the ϵ estimations (see discussions in the above paragraph), however, it is still difficult to fully rule out the existence of an intrinsic ϵ_t - $M_{\bullet, t}$ correlation just by comparing the results obtained from the SDSS QSOs with that obtained from such mock samples. We conclude that the intrinsic correlation between the radiative efficiency and the true MBH mass, if any, must be much weaker than the apparent correlation between ϵ and $M_{\bullet, \text{vir}}$ found for the SDSS sample in each redshift bin.

To close this section, we conclude that the strong correlations between ϵ and $M_{\bullet, \text{vir}}$ found in section 3 can be produced by and mainly due to the selection effects of the SDSS QSO sample and the biases in the ϵ estimations induced by the usage of $M_{\bullet, \text{vir}}$ as the true MBH mass. By studying a number of QSOs (or AGNs) with different luminosities and MBH masses and redshifts, Raimundo et al. (2012) find that the ϵ - $M_{\bullet, \text{vir}}$ relation found by Davis & Laor (2011) may be an artifact of the small parameter space covered by the DL sample. With the large data set of the SDSS QSO catalog, we have demonstrated that a correlation between ϵ - $M_{\bullet, \text{vir}}$ can be generated by mocking SDSS QSOs through modelling various selection effects and biases (though there is no input intrinsic correlation between ϵ - $M_{\bullet, t}$), and our results are consistent with that of Raimundo et al. (2012). Note that the empirical SED of QSOs, more or less uniform, is adopted to calculate the bolometric luminosity of each SDSS QSO in section 3.2. As argued in Laor & Davis (2011), the small spread in the SED shape is an intriguing question that currently does not have a simple answer.

5 CONCLUSIONS

Radiative efficiencies of the disk accretion processes in individual QSOs are related to the spins of the central MBHs, which may be profoundly connected to the MBH assembly history as suggested by a number of recent studies (e.g., Gammie et al. 2004; Volonteri et al. 2005; King & Pringle 2006; King et al. 2008; Berti & Volonteri 2008; Dubois et al. 2013). It is therefore of great importance to estimate the radiative efficiency of individual QSOs and investigate its statistical distribution among QSOs. In this study, we estimate the radiative efficiency individually for a large number of SDSS QSOs. We first estimate the accretion rate for each QSO by matching the detected optical band luminosity(/-ies) with that predicted by the disk model, by adopting the thin disk accretion model and assuming that the true mass of the central MBH is the same as that given by the virial mass estimator(s). We also estimate the bolometric luminosity of each QSO by adopting the empirical spectral energy distribution suggested by various multi-wavelength observations of small QSO samples. With the estimated accretion rate and the bolometric luminosity, we obtain the radiative efficiency for each SDSS QSO. We find an apparent strong correlation between the radiative efficiency and the MBH

virial mass in low redshift bins and it becomes weak in high redshift bins. In the lowest redshift bin ($0.3 \leq z < 0.5$), this apparent correlation ($\epsilon \propto M_{\bullet, \text{vir}}^\beta$, and $\beta \sim 0.56 - 0.64$) is roughly consistent with that found by Davis & Laor (2011) for the DL QSOs in a similar redshift range. We also find that the mean radiative efficiencies of the SDSS QSOs are consistent with being a constant $\simeq 0.11 - 0.16$ (though with large scatters) over the redshift range from 0.3 to 4, which does not suggest any significant evolution with redshift. This estimate of the mean radiative efficiency of QSOs is totally independent of but roughly consistent with those estimations based on the Soltan argument (e.g., Yu & Tremaine 2002; Yu & Lu 2004; Marconi et al. 2004; Yu & Lu 2008; Shankar et al. 2009; Zhang et al. 2012; Shankar et al. 2013).

With the enormous large sample of the SDSS QSOs, it is possible to statistically model the various biases in the estimations of the radiative efficiency and the selection effects of the SDSS QSOs. To do so, we generate mock SDSS QSO samples according to the true MBH mass function and the Eddington ratio distribution obtained in Kelly & Shen (2013), by involving the selection criteria of the SDSS QSOs and the uncertainties in the MBH virial mass estimations and the inclination angles. We estimate the radiative efficiency for QSOs in each mock sample by adopting the same method as that for the SDSS QSO and obtain the probability density distribution of those mock QSOs in the radiative efficiency versus the MBH virial mass plane. We find that the ϵ - $M_{\bullet, \text{vir}}$ correlations for the SDSS QSOs in different redshift bins can be well explained by the selection effects and the biases induced by the usage of $M_{\bullet, \text{vir}}$ as the true MBH mass, and the selection effects play the dominant roles in leading to the ϵ - $M_{\bullet, \text{vir}}$ correlation, as suggested by Raimundo et al. (2012). We conclude that the current SDSS QSO data is consistent with no intrinsic correlation between the QSO radiative efficiency and the true MBH mass.

In principle, the accretion rate of a QSO may be better determined by fitting the QSO spectrum covering a wide range of wavelengths (e.g., from the infrared band to the hard X-ray band), through an elaborate accretion disk model, and the constraints on the MBH spin and consequently the radiative efficiency may be also simultaneously obtained. In the future, if observations can obtain the spectra for a large sample of QSOs, with good wavelength, luminosity and redshift coverage, it may be possible to estimate their radiative efficiencies in a more self-consistent way and then further investigate the relationship, if any, between the radiative efficiency and the MBH mass, which would shed light on not only the assembly history of MBHs (e.g., Dubois et al. 2013) but also the physical reasons for the small spread in the SED shapes of QSOs pointed by Laor & Davis (2011).

Acknowledgments

We thank Qingjuan Yu for constructive suggestions and discussions, Andreas Schulze and Changshuo Yan for helpful discussions. This work was supported in part by the National Natural Science Foundation of China under nos. 10973017 and 11033001, the National Basic Research Program (973 Programme) of China (Grant 2009CB824800), and the BaiRen program from the National Astronomical Observatory of China, Chinese Academy of Sciences.

REFERENCES

- Berti, E., Volonteri, M., 2008, *ApJ*, 684, 822
- Blandford, R. D., McKee, C. F., 1982, *ApJ*, 255, 419
- Cao, X., Li, F., 2008, *MNRAS*, 390, 561
- Chelouche, D., 2013, *arXiv:1305.6507*
- Collin, S., Boisson, C., Mouchet, M., et al., 2002, *A&A*, 388, 771
- Davis, S. W., Hubeny, I., 2006, *ApJS*, 164, 530
- Davis, S. W., Laor, A., 2011, *ApJ*, 728, 98
- Dubois, Y., Volonteri, M., Silk, J., 2013, *arXiv:1304.4583*
- Elvis, M., Wilkes, B. J., McDowell, J. C., et al., 1994, *ApJS*, 95, 1
- Fabian, A. C., Iwasawa, K., Reynolds, C. S., Young, A. J., 2000, *PASP*, 112, 1145
- Gammie, C. F., Shapiro, S. L., McKinney, J. C., 2004, *ApJ*, 602, L312
- Gierliński, M., Maciolek-Niedzwiecki, A., Ebisawa, K., 2001, *MNRAS*, 325, 1253
- Hopkins, P. F., Richards, G. T., Hernquist, L., 2007, *ApJ*, 654, 731
- Hubeny, I., Agol, E., Blaes, O., Krolik, J. H., 2000, *ApJ*, 533, 710
- Hubeny, I., Lanz, T., 1995, *ApJ*, 439, 875
- Hughes, S. A., Blandford, R. D., 2003, *ApJ*, 585, L101
- Jin, C., Ward, M., Done, C., Gelbord, J., 2012, *MNRAS*, 420, 1825
- Kaspi, S., Smith, P. S., Netzer, H., Maoz, D., Jannuzi, B. T., Giveon, U., 2000, *ApJ*, 633, 631
- Kelly, B. C., Shen, Y., 2013, *ApJ*, 764, 45
- King, A. R., Pringle, J. E., 2006, *MNRAS*, 373, L90
- King, A. R., Pringle, J. E., Hofmann, J. A., 2008, *MNRAS*, 385, 1621
- Krolik, J. H., 1999, *Active Galactic Nuclei: from the central black hole to the galactic environment* (Princeton, Princeton University Press)
- Laor, A., Davis, S., 2011, *arXiv:1110.0653*
- Li, Y. R., Wang, J. M., Ho, L. C., 2012, *ApJ*, 749, 187
- Lusso, E., Comastri, A., Vignali, C., et al., 2010, *A&A*, 512, 34
- Magdziarz, P., Zdziarski, A. A., 1995, *MNRAS*, 273, 837
- Marconi, A., Risaliti, G., Gillin, R., Hunt, L. K., Maiolino, R., & Salvati, M., 2004, *MNRAS*, 351, 169
- Novikov, I. D., Thorne, K. S., 1973, in *Black Holes*, ed. C. De Witt & B. De Witt (New York: Gordon & Breach), 343
- Page, D. N., Thorne, K. S., 1974, *ApJ*, 191, 499
- Peterson, B. M., Ferrarese, L., Gilbert, K. M., et al., 2004, *ApJ*, 613, 682
- Raimundo, S. I., Fabian, A. C., Vasudevan, R. V., Gandhi, P., Wu, J., 2012, *MNRAS*, 419, 2529
- Reynolds, C. S., 2013a, *arXiv:1302.3260*
- Reynolds, C. S., 2013b, *arXiv:1307.3246*
- Richards, G. T., Fan, X., Newberg, H. J., et al., 2002, *AJ*, 123, 2945
- Richards, G. T., Lacy, M., Storrie-Lombardi, L. J., et al., 2006a, *ApJS*, 166, 470
- Richards, G. T., Strauss, M. A., Fan, X., et al., 2006b, *AJ*, 131, 2766
- Risaliti, G., Harrison, F. A., Madsen, K. K., et al. 2013, *Nature*, 494, 449
- Runnoe, J. C., Brotherton, M. S., Shang, Z., 2012, *MNRAS*, 422, 478
- Shakura, N. I., Sunyaev, R. A., 1973, *A&A*, 24, 337
- Shankar, F., Weinberg, D. H., Miralda-Escudé, J., 2009, *ApJ*, 690, 20
- Shankar, F., Weinberg, D. H., Miralda-Escudé, J., 2013, *MNRAS*, 428, 421
- Shen, Y., Greene, J. F., Strauss, M. A., Richards, G. T., Schneider, D. P., 2008, *ApJ*, 680, 169
- Shen, Y., Richards, G. T., Strauss, M. A., et al. 2011, *ApJS*, 194, 45
- Small, T. A., Blandford, R. D., 1992, *MNRAS*, 259, 725
- Sołtan, A., 1982, *MNRAS*, 200, 115
- Steffen, A. T., Strateva, I., Brandt, W. N., et al., 2006, *AJ*, 131, 2826
- Sun, W. H., Malkan, M. A., 1989, *ApJ*, 346, 68
- Telfer, R. C., Zheng, W., Kriss, G. A., Davidsen, A. F., 2002, *ApJ*, 565, 773
- Tozzi, P., Gilli, R., Mainieri, V., et al., 2006, *A&A*, 451, 457
- Vanden Berk, D. E., Richards, G. T., Bauer, A., et al., 2001, *AJ*, 122, 549
- Vasudevan, R. V., Fabian, A. C., 2007, *MNRAS*, 381, 1235
- Vasudevan, R. V., Fabian, A. C., 2009, *MNRAS*, 392, 1124
- Vestergaard, M., 2002, *ApJ*, 571, 733
- Vestergaard, M., Peterson, B. M., 2006, *ApJ*, 641, 689
- Volonteri, M., Madau, P., Quataert, E., Rees, M. J., 2005, *ApJ*, 620, 69
- Volonteri, M., Sikora, M., Lasota, J.-P., & Merloni, A. 2012, *arXiv:1210.1025*
- Wang, J.-M., Hu, C., Li, Y., et al., 2009, *ApJL*, 697, L141
- Yu, Q., Lu, Y., 2004, *ApJ*, 602, 603
- Yu, Q., Lu, Y., 2008, *ApJ*, 689, 732
- Yu, Q., Tremaine, S., 2002, *MNRAS*, 335, 965
- Zhang, X., Lu, Y., & Yu, Q. 2012, *ApJ*, 761, 5